Version: 2009 January 15

The distance to a star forming region in the Outer arm of the Galaxy

K. Hachisuka[1,2], A. Brunthaler[2], K. M. Menten[2], M. J. Reid[3],
Y. Hagiwara[4] and N. Mochizuki[5]

ABSTRACT

We performed astrometric observations with the VLBA of WB89−437, an H_2O maser source in the Outer spiral arm of the Galaxy. We measure an annual parallax of 0.167±0.006 mas, corresponding to a heliocentric distance of 6.0±0.2 kpc or a Galactocentric distance of 13.4 ± 0.2 kpc. This value for the heliocentric distance is considerably smaller than the kinematic distance of 8.6 kpc. This confirms the presence of a faint Outer arm toward $l = 135°$. We also measured the full space motion of the object and find a large peculiar motion of $\sim$20 km s^{-1} toward the Galactic center. This peculiar motion explains the large error in the kinematic distance estimate. We also find that WB89−437 has the same rotation speed as the LSR, providing more evidence for a flat rotation curve and thus the presence of dark matter in the outer Galaxy.

Subject headings: astrometry, masers, stars: distances, Galaxy: structure, kinematics and dynamics

1. Introduction

The Outer spiral arm of the Milky Way (also called the Cygnus arm) is located beyond the Perseus arm and may be the outermost arm of the Galaxy's stellar disk (see Fig. 1). It

[1]Key Laboratory for Research in Galaxies and Cosmology, Shanghai Astronomical Observatory, Chinese Academy of Science, Shanghai, 200030, China

[2]Max-Planck-Institut für Radioastronomie, Auf dem Hügel 69, Bonn, 53121, Germany

[3]Harvard-Smithsonian Center for Astrophysics, 60 Garden Street, Cambridge, MA 02138, USA

[4]National Astronomical Observatory, Mitaka, Tokyo 181-8588, Japan

[5]Institute of Space and Astronautical Science, Japan Aerospace Exploration Agency, 3-1-1 Yoshinodai, Sagamihara, Kanagawa, 229-8510, Japan

is traceable across portions of the fourth and first quadrants of the Galaxy and it can be detected through the emission of HI and molecular gas (Nakanishi & Sofue 2003; Nakanishi & Sofue 2006). The arm may continue through the second and third quadrants, as shown by spectroscopic and photometric observations of open clusters (Pandey et al. 2006) and HII regions (Russeil et al. 2007). Indeed, Honma et al. (2007) used the VERA array and measured the annual parallax and proper motion of H_2O masers in S 269, a star forming region at a Galactic longitude of 196°. They found a Galactocentric distance of 13.6 kpc (for R_0=8.5 kpc), consistent with it being in the Outer arm.

The size and structure of our Galaxy have been mainly determined by kinematic distances, which involve comparing measured radial velocities with a kinematic model (e.g., Gómez 2006). However, kinematic distances depend strongly on the Galactic rotation model chosen and peculiar motions render them questionable (e.g., Xu et al. 2006). This is particularly true for the outer Galaxy, since the Galactic rotation speed is quite uncertain (e.g. Brand & Blitz 1993).

Recently, distances of Galactic maser sources have been directly determined by annual parallax measurements that use phase-referencing VLBI techniques (e.g. Hachisuka et al. 2006; Xu et al. 2006; Honma et al. 2007). Such parallax measurements can yield distances of many kiloparsecs with errors less than ten percent, allowing *direct* distance determinations for objects located near the edge of the stellar disk of our Galaxy.

Wouterloot et al. (1993) searched for H_2O maser sources toward IRAS sources with ^{12}CO emission and found several for which their kinematic distances indicated large distances from the Galactic center. Most of these maser sources seem to be located in the Perseus arm, but several sources have large negative LSR velocities and are probably in the Outer arm (Wouterloot et al. 1995).

One of these sources, WB89−437 (IRAS 02395+6244), is located at a Galactic longitude of $l = 135°$ and has a kinematic distance of 8.6 kpc, which would place it beyond the Outer arm. It is one of the most luminous FIR source with the strongest H_2O maser emission in the outer part of the Galaxy. Since radio continuum emission has not been detected, the spectral type of the exciting star is thought to be B1 (Rudolph et al. 1996) or later (Brand et al. 2001). The young stellar object WB89−437 itself is deeply embedded and, testifying for its youth, drives an outflow traced by high velocity CO and H_2O masers. The latter are found offset by roughly 3 arcseconds from the position of the peak of CO and CS emission.

Because of its strength and location in the outer part of the Galaxy, we selected this maser as the target for an annual parallax measurement. Here we report the results of these measurements, which yielded the distance and proper motion of this star forming region in

the outer part of the Galaxy.

2. Observation and data reduction

We used the NRAO[1] Very Long Baseline Array (VLBA) to observe WB89−437 under program BH136. The observations involved rapid switching between an extragalactic background continuum radio source and the H_2O maser. The observations were performed at 5 epochs spread over about 10 months in 2006 (see Table 1 for details). The separations between adjacent epochs were typically 3 months and the observations were performed close to the dates of the maximum and minimum of the annual parallax signature in right ascension and declination. We limited the observing time span to 10 months, instead of 1 year, to minimize the effects of maser variability.

We observed two 16 MHz wide bands with one band centered on the maser's centroid LSR velocity of -70.0 km s^{-1}. The data were correlated with 1024 spectral channels in each band, resulting in a channel spacing of 0.21 km s^{-1}. We used the ICRF extragalactic radio source J0244+6228 at R.A.=$02^h44^m57.696849\pm0.000168^s$ and Dec.=$+62°28'06.51470\pm0.00097''$ (J2000) (Fey et al. 2004) as the phase-reference source. This source had already been used for the parallax observation of the H_2O maser in W3OH (Hachisuka et al. 2006). J0244+6228 had no detectable extended structure and its high flux density, near 1 Jy at 22 GHz, makes it an excellent source for phase-referencing VLBI. Moreover, its angular separation from WB89−437 is only $0°.5$, promising high quality relative astrometry. We switched between maser and reference source every 30 seconds, yielding ≈22 seconds on-source time per scan. At each epoch, we obtained total on-source integration times of ≈ 50 minutes for each source. The total observing time was spread over 6 hours, including the calibrator observations, the slewing time of the telescopes, and observations of a second maser which will be presented elsewhere.

In order to correct for small zenith delay errors in the atmospheric model of the VLBA correlator (see Reid & Brunthaler 2004), we performed *geodetic-like* observations at 22 GHz (Brunthaler et al. 2005) at the beginning and end of each VLBA observation. These observations involved 22 ICRF sources with positions accurate to better than 1 mas and sampled a wide range of source elevations with a frequency setup involving eight 4 MHz bands at left circular polarization that spanned a frequency range of 450 MHz. The multi-band delays and rates from a fringe fit to these quasars were then fit with a model that consisted of a

[1]The National Radio Astronomy Observatory is a facility of the National Science Foundation operated under cooperative agreement by Associated Universities, Inc.

zenith delay offset at all antennas as well as a clock offset at all antennas except the reference antenna.

Most of the calibration and data reduction were carried out with standard procedures for spectral-line observations using the NRAO's Astronomical Image Processing System (AIPS). First, we applied the latest values of the Earth's orientation parameters and corrected for effects of the changing feed parallactic angles. Next, we removed atmospheric zenith delay errors, corrected for voltage offset in the samplers, and applied antenna gains and system temperatures for the amplitude calibration. Next, we corrected for electronic delay and phase differences among the IF bands using data from NRAO 150. Many H_2O maser spots could be imaged after calibration. We determined their peak positions on images by fitting elliptical Gaussian components and traced individual maser spots over the five epochs.

3. Results

Twenty H_2O maser features were detected in the LSR velocity range -62 to -76 km s^{-1}, distributed over an area of $0''.8 \times 1''.6$ (Fig. 2). 16 of the 20 H_2O maser features were detected at 2 or more epochs and 4 of them were detected at all 5 epochs. We used three of the four H_2O maser features that were detected at all five epochs for the parallax fitting. The last feature was located at a distance of $\sim 1.4''$ from the phase center, which is larger than our nominal field of view ($\sim 0.7''$). Hence, it was heavily affected by fringe-rate smearing and was not used for the parallax estimate.

3.1. Annual parallax and distance

One maser feature was detected in thirty channels, and two features were detected over seven frequency channels. First, we fitted the parallaxes and proper motions to data from each spectral channel individually. The residuals to the fits showed reduced χ^2 values that were relatively large ($\sim$ 2–8), since the formal position errors from the Gaussian fits to the maps underestimate the true position uncertainty. The true position error of a maser spot relative to a background source is usually dominated by systematics, owing to uncalibrated residual atmospheric delays and/or maser spot structural variations. Hence, we added "error floors" in quadrature to the formal position uncertainties until we achieved χ^2 per degree of freedom values of near unity for the data from each coordinate. For this dataset we needed error floors between 10 and 60 μas for different maser features. The individual parallaxes and proper motions for each feature are shown in Table 2 together with their formal errors from

the fit. Also given are the average parallaxes and proper motions for each feature together with the standard error of the mean and the standard deviation (in parentheses).

Next, we fitted all channels from any given maser feature simultaneously with one parallax but different proper motions and position offsets for each channel. The resulting parallaxes for each maser feature are also given in Table 2. All three features have consistent parallaxes of 0.164±0.0014, 0.163±0.004 mas and 0.164±0.007 mas. We also performed a combined parallax fit with all channels from the three features. The resulting parallax is 0.164±0.0016 mas. For this fit we used error floors of 17 and 12 μas in right ascension and declination, respectively. Fig. 3 (top) shows the parallax signal for one channel (i.e. the first channel) from each feature and the combined fit to all channels. The individual proper motions and position offsets were removed before plotting.

Combining the results of several maser spots can lead to underestimation of the parallax uncertainty, since the measurements may not be statistically independent. Random-like errors (e.g. from map noise and possibly maser spot structure variations) will not be correlated among different maser spots. However, systematic errors (e.g. caused by residual atmospheric delay errors) will affect all maser spots in one epoch in a very similar way. The most conservative approach would be to assume 100% correlation and multiply the formal error by $\sqrt{N}$, where N is the number of individual data sets used in the fit. This would give an error of $\sqrt{44} \times 0.0016$ mas = 0.011 mas.

To estimate the effect of the systematic errors on our parallax measurement, we examined position residuals after removing the proper motions and position offsets (e.g. the data plotted in Fig. 3, top) and calculated the average maser position of all channels from all three features in each epoch. The averaging should reduce the random error, but leave the systematic error unaffected. A parallax fit to the averaged data points (Fig. 3, bottom) yielded a value of 0.167±0.003 mas, which is consistent with the value from the combined fit. Here we used error floors of 12 and 5 μas in right ascension and declination, respectively, to achieve χ^2 values of ∼1. This suggests that the systematic errors are larger in right ascension, contrary to our previous experience, where systematic errors in declination dominate. However, because the source is at high declination, systematic errors in right ascension may dominate in such a case for some geometrical configurations (Pradel et al. 2006). Furthermore, the 8.6 GHz image of the calibrator J0244+6228 in the VLBA calibrator tool shows a weak jet mainly directed toward the east. Thus, small changes in this jet could introduce larger systematic errors in right ascension than in declination. The different error floors are also the reason why the parallax fit to the averaged data is slightly larger than the parallax fits to the individual features.

In order to allow for errors induced by the VLBI structure of the reference quasar, we

multiply our final error by a factor of two and obtain 0.167±0.006 mas, which we adopt for the parallax of WB89−437. This parallax corresponds to a distance of 6.0 ± 0.2 kpc from the Sun, or a Galactocentric distance of 13.4 ± 0.2 kpc (assuming R_0=8.5 kpc).

3.2. Proper motion and full space motion in the Galaxy

Since we have a distance, proper motion and radial velocity, we can determine the 3-dimensional motion of WB89−437 in the Galaxy. The absolute proper motion of a Galactic object relative to an extragalactic source depends not only on the annual parallax but also on differential Galactic rotation, the Solar Motion and the peculiar motion (relative to Galactic rotation) of the object. In addition, H_2O masers in star forming regions usually participate in outflows with typical velocities of a few tens of km s^{-1}. Therefore, the absolute proper motions and radial velocities of maser spots can contain a significant component from internal motions.

The absolute proper motions of the three maser features range from −1.18 to −1.35 mas $year^{-1}$ in right ascension and from 0.59 to 1.05 mas $year^{-1}$ in declination. The average motion of these features is -1.27 ± 0.05 mas $year^{-1}$ in right ascension and 0.82 ± 0.13 mas $year^{-1}$ in declination. However, it is not clear that the average proper motion of the three maser spots represent the true motion of the whole object.

To evaluate the effect of relative internal motions, we calculated the average motion of 11 maser features relative to a reference feature (maser spot 2 with an LSR velocity of −73.16 km s^{-1}). Here we used all maser spots which were detected in at least two epochs and not affected by fringe-rate smearing. The results are shown in Fig. 2 and Table 3. Also given is the average proper motion together with the standard error of the mean and the standard deviation (in parentheses). The average motion is -0.02 ± 0.15 mas $year^{-1}$ in right ascension and -0.35 ± 0.18 mas $year^{-1}$ in declination. The true proper motion of the whole source can then be estimated by the sum of the average motion and the absolute proper motion of the reference feature. This gives a total motion of -1.22 ± 0.30 mas $year^{-1}$ in right ascension and 0.46 ± 0.36 mas $year^{-1}$ in declination. Here we also multiplied the final error by a factor of two to allow for errors induced by the background quasar.

We assume IAU values for the distance of the Sun from the Galactic center of R_0=8.5 kpc and the circular rotation speed of the LSR of Θ_0=220 km s^{-1}. We also adopt the Solar Motion with respect to the LSR in km s^{-1} from HIPPARCOS data, (U,V,W) = $(10.00 \pm 0.36, 5.25 \pm 0.62, 7.17 \pm 0.38)$ (Dehnen & Binney 1998). Then our distance measurement of 6.0±0.2 kpc, the proper motion of −1.22±0.30 mas $year^{-1}$ in right ascension and 0.46±0.36 mas $year^{-1}$ in

declination, and a radial velocity of -72 ± 2 km s^{-1} from CO and CS measurements (Brand et al. 2001), which should be close to the stellar velocity, implies a peculiar motion relative to a circular Galactic rotation of:

$$\begin{aligned} U' &= 23.1 \pm 4.1\,\mathrm{km\,s^{-1}}, \\ V' &= -3.6 \pm 7.9\,\mathrm{km\,s^{-1}}, \\ W' &= 0.8 \pm 9.9\,\mathrm{km\,s^{-1}}. \end{aligned}$$

Here, U' denotes the velocity component toward the Galactic Center, V' is the component in direction of Galactic rotation, and W' is the component toward the North Galactic Pole.

If one uses a different rotation model of the Milky Way with R_0=8.0 kpc and Θ_0=236 km s^{-1}, which is consistent with the measured proper motion of the Galactic center super-massive black hole, Sgr A* (Reid & Brunthaler 2004), we get

$$\begin{aligned} U' &= 15.2 \pm 4.1\,\mathrm{km\,s^{-1}}, \\ V' &= -4.2 \pm 8.0\,\mathrm{km\,s^{-1}}, \\ W' &= 0.8 \pm 9.9\,\mathrm{km\,s^{-1}}. \end{aligned}$$

Hence, WB89−437 rotates in both cases with the approximately same velocity as the LSR but shows a large peculiar motion of ≈ 20 km s^{-1} toward the Galactic center.

4. Discussion

4.1. WB89−437 in the outer Galaxy

The Galactocentric distance of WB89−437 is 13.4 kpc (for R_0=8.5 kpc), which places the source well outside the Perseus spiral arm, which is at a Galactocentric distance of ≈ 10.0 kpc in this direction (Xu et al. 2006, Hachisuka et al. 2006). While the distribution of molecular gas in the outer Galaxy shows that the Outer arm becomes much weaker near $l = 90°$ (Nakanishi & Sofue 2006), some CO clouds with high radial velocities are distributed from $l = 131°$ to 137° (Digel et al. 1996). This indicates that WB89−437 (at $l = 135°$) is located in a weak extension of the Outer arm. Potential arm objects at $l > 137°$ have been identified (Russeil et al. 2007) which suggest that this faint arm continues to the third Galactic quadrant. This view is supported by Honma et al. (2007) who used the VERA array

and measured the annual parallax and proper motion of a H_2O maser at a Galactic longitude of 196°. They found a Galactocentric distance of 13.6 kpc (for R_0=8.5 kpc), consistent with it being in the Outer arm. There are many maser sources at the outer Galaxy whose annual parallax have not been measured. With direct measurements of distances to these sources, we may understand the structure of the Outer (and the Perseus) arm in more detail.

With a Galactic latitude of $b = 2.8°$ and a distance of 6 kpc, WB89-437 is located ∼300 pc above the Galactic plane. With our upper limit of 10 km s^{-1} for the motion perpendicular to the plane, it would have needed more than 30 million years to reach its current position. This is much larger than the age of this object. Thus, WB89-437 must have formed already far above the plane.

4.2. Galactic dynamics in the Outer arm

The annual parallax distance to WB89−437 (6.0±0.2 kpc) is significantly smaller than its kinematic distance of 8.6±0.4 kpc, assuming recommended IAU values R_0 and Θ_0. However, we note that our measured distance is in slightly better agreement with the kinematic distance of 7.3±0.3 kpc that one obtains for R_0=8.0 kpc and Θ_0=236 km s^{-1} (Reid & Brunthaler 2004), but there is still a significant discrepancy. The large peculiar motion of WB89−437 of ∼20 km s^{-1} toward the Galactic center has a component of ∼10 km s^{-1} toward the Sun and is partially responsible for this discrepancy.

This is similar to the case of W3OH (Xu et al. 2006 ; Hachisuka et al. 2006), which is located at a similar Galactic longitude but is in the Perseus arm. W3OH also shows a large peculiar motion and a true distance which is smaller than the kinematic distance. Anomalous motions in the Perseus arm are well known to exist (Humphreys 1978); they could be caused by spiral density waves. On the other hand, since the outer arm in the Galaxy is a faint arm, one expects that the influence of a density wave on it is smaller than on an inner arm. In fact, spiral structure of HI gas at large Galactic radii (>25 kpc) is not seen (Levine et al. 2006).

A flat rotation curve of the outer Galaxy implies the existence of dark matter since the density of visible matter in the outer Galaxy is smaller than in the inner Galaxy. The measured circular orbital speed of WB89−437 is consistent with that of the LSR. This confirms the result of Honma et al. (2007) that the rotation curve of the Milky Way is constant out to ∼13.5 kpc and provides more solid evidence for the existence of dark matter in the outer region of the Galaxy. However, since massive star forming regions can have large peculiar motions, it may be possible, although unlikely, that the rotation curve falls by ∼ 20

km s^{-1} between the Sun and the Outer arm, but the source has a compensating component in the direction of Galactic rotation.

5. Conclusion

We performed astrometric VLBA observations toward the Galactic H_2O maser source WB89−437 in the Outer arm of the Galaxy. The measured annual parallax of 0.167±0.006 mas corresponds to a heliocentric distance of 6.0±0.2 kpc (a Galactocentric distance of 13.4 ± 0.2 kpc). This confirms the presence of a faint Outer arm in the direction of $l = 135°$. Our measured distance is smaller than the kinematic distance of 8.6 kpc. We also estimate the 3D motion of the object with respect to a Galactic reference frame and find that the discrepancy between kinematic distance and true distance is caused, in part, by a large peculiar motion of ∼20 km s^{-1} toward the Galactic center. We also find that WB89-437 has the same rotation speed as the LSR, confirming a flat rotation curve in the outer Galaxy.

This work was supported in part by the National Natural Science Foundation of China (grants 10573029, 10625314, 10633010 and 10821302) and the Knowledge Innovation Program of the Chinese Academy of Sciences (Grant No. KJCX2-YW-T03), and the National Key Basic Research Development Program of China (No. 2007CB815405). KH acknowledges the support by China Postdoctoral Science Foundation (grant 20070410745). Andreas Brunthaler was supported by the DFG Priority Programme 1177.

REFERENCES

Benjamin, R. A., Churchwell, E., Babler, B. L. et al., 2005, ApJ, 630, 149

Banjamin, R. A., 2008, ASP Conference Series, Vol. 387, p. 375

Brand, J. and Blitz, L., 1993, A&A, 275, 67

Brand, J., Wouterloot, J. G. A., Rudolph, A. L. and de Geus, E. J., 2001, A&A, 377, 644

Brunthaler, A., Reid, M. J. and Falcke, H., 2005, Future Directions in High Resolution Astronomy: The 10th Anniversary of the VLBA, ASP Conference Proceedings, Vol. 340. Edited by J. Romney and M. Reid., 455

Dehnen, W. and Binney, J. J., 1998, MNRAS, 298, 387

Digel, S. W., Lyder, D. A., Philbrick, A. J. et al., 1996, ApJ, 458, 561

Fey, A. L., Ma, C., Arias, E. F. et al., 2004, AJ, 127, 3587

Georgelin, Y. M.& Georgelin, Y. P., 1976, A&A, 49, 57

Gómez, G. C., 2006, AJ, 132, 2376

Hachisuka, K., Brunthaler, A., Menten, K. M., Reid, M. J. et al., 2006, ApJ, 645, 337

Honma, M., Bushimata, T., Choi, Y. K. et al., 2007, PASJ, 59, 889

Humphreys, R. M., 1978, ApJS, 38, 309

Levine, E. S., Blitz, L. and Heiles, C., 2006, Science, 312, 5781

Nakanishi, H. and Sofue, Y., 2003, PASJ, 55, 191

Nakanishi, H. and Sofue, Y., 2006, PASJ, 58, 847

Pandey, A. K., Sharma, S. and Ogura, K., 2006, MNRAS, 373, 255

Pradel, N., Charlot, P. and Lestrade, J.-F., 2006, A&A, 452, 1099

Reid, M. J., 1993, ARA&A, 31, 345

Reid, M. J. and Brunthaler, A., 2004, ApJ, 616, 872

Rudolph, Alexander L., Brand, J., de Geus, E. J. and Wouterloot, J. G. A., 1996, ApJ, 458, 653

Russeil, D., 2003, A&A, 397, 133

Russeil, D., Adami, C. and Georgelin, Y. M., 2007, A&A, 470, 161

Wouterloot, J. G. A., Brand, J. and Fiegle, K., 1993, A&AS, 98, 589

Wouterloot, J. G. A., Fiegle, K., Brand, J. and Winnewisser, G., 1995, A&A, 301, 236

Xu, Y., Reid, M. J., Zheng, X. W. and Menten, K. M., 2006, *Science*, 311, 54

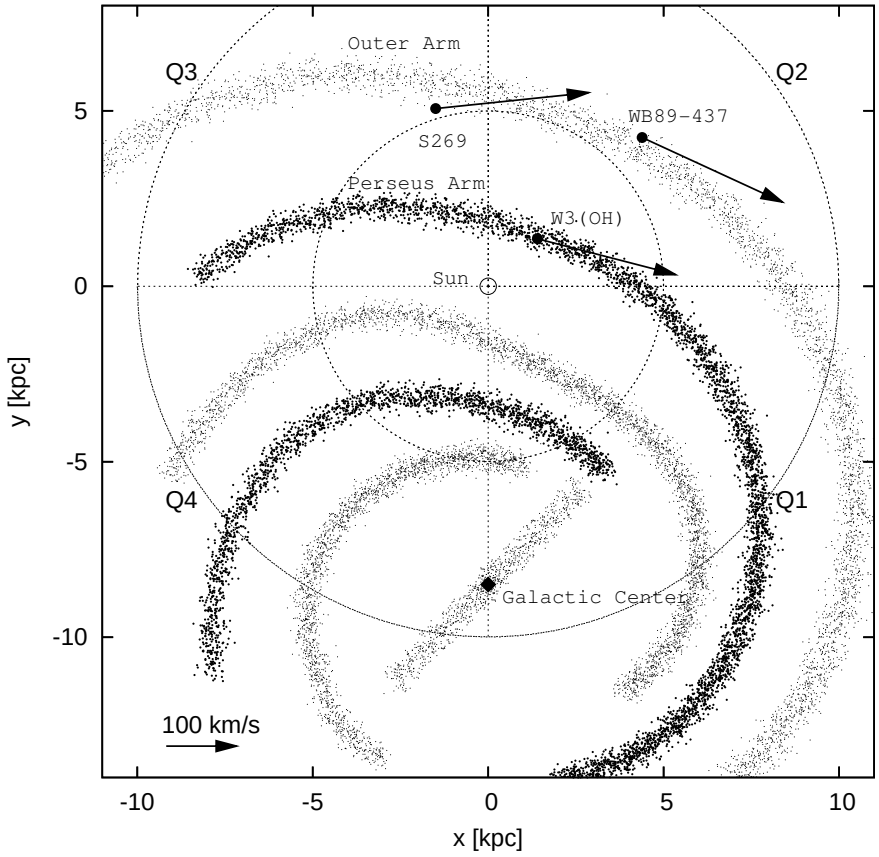

Fig. 1.— Schematic view of the spiral arms of the Milky Way (Georgelin & Georgelin 1976) with the positions of W3OH (Xu et al. 2006; Hachisuka et al. 2006), S269 (Honma et al. 2007), WB89-437 (this paper), and their motions relative to the Galactic Center (arrows). The IAU value R_0=8.5 kpc was assumed. Two dark arms represent principal arms, namely the Perseus and Scutum-Centaurus arm (Benjamin 2008). Also shown is the location of the central bar from Benjamin et al. (2005). The labels Q1-Q4 designate the standard four quadrants of the Galaxy.

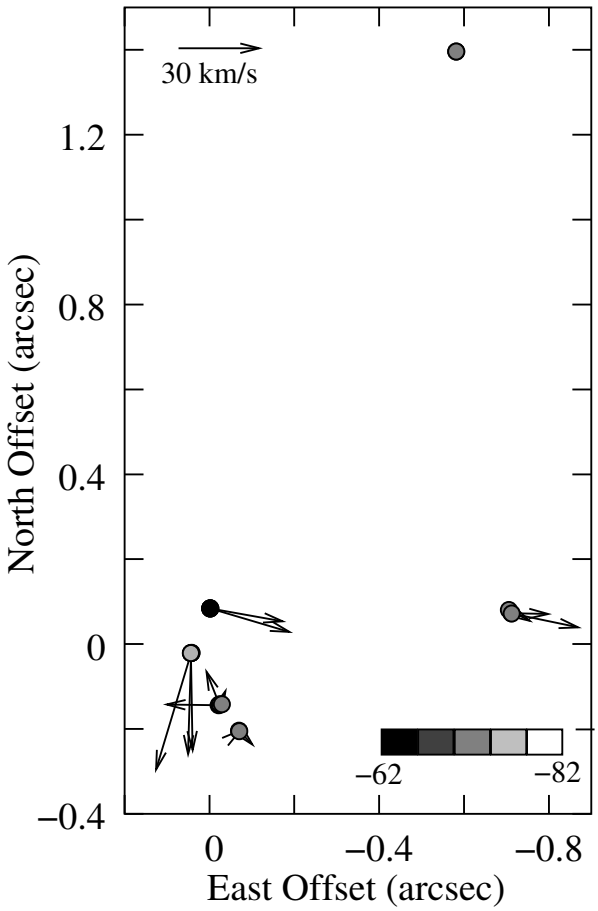

Fig. 2.— Spot distribution (circles) and internal motions not affected by fringe-rate smearing (arrows) relative to a positional reference feature (maser spot 2 with a LSR velocity of -73.16 km s^{-1} in Table 2.) of maser components that were detected at two or more epochs. The coordinate of the origin of the map is $02^h43^m28.5680^s$, $62°57'08.388''$ (J2000). The gray scale indicates radial velocities as coded in the panel at the lower right. The radial velocity of thermally emitting molecular lines is -72 km s^{-1}.

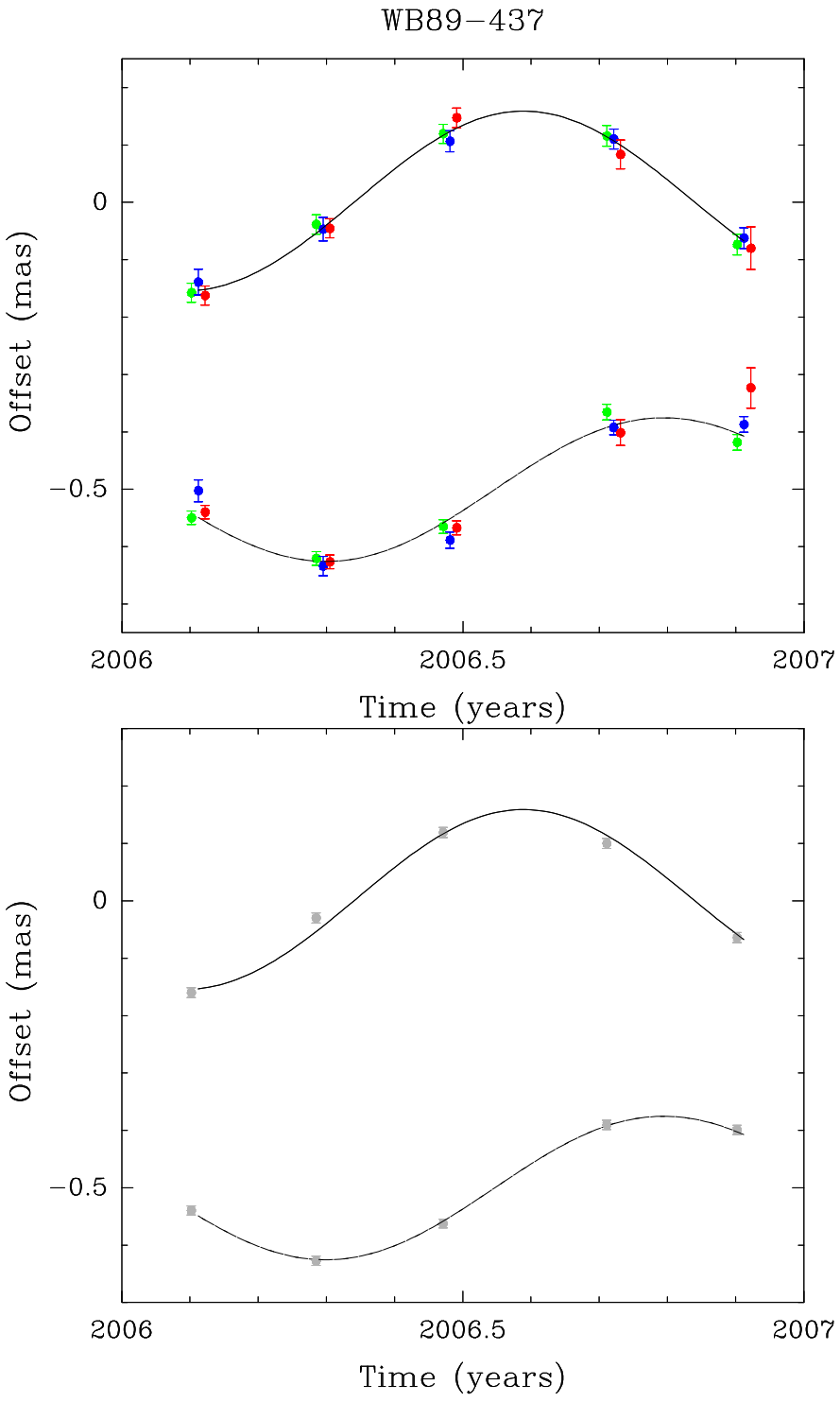

Fig. 3.— **Top:** Annual parallax signal of one channel (i.e. the first channel) from each maser feature in WB89−437. The individual proper motions and position offsets are removed. The data for the different maser features are slightly shifted in time for clarity (green: maser feature 1, blue: feature 2, red: feature 3). The upper data shows the parallax in east-west direction while the lower data shows the parallax in north-south direction. **Bottom:** Annual parallax signal for the average positions of the data from all channels from the three maser spots after removing the individual proper motions and position offsets. The upper data shows the parallax in east-west direction while the lower data shows the parallax in north-south direction.

Table 1. Details of the VLBA observations

Date	J0244+6228 Flux density (mJy)	Beam HPBW; P.A (mas^2); (°)	Image rms per channel ($mJy\,bm^{-1}$)
2006 Feb 09	443	0.79×0.28; 11	12
2006 Apr 17	758	0.80×0.27; 12	12
2006 Jun 24	852	0.80×0.28; 11	16
2006 Sep 20	1244	0.80×0.28; 10	17
2006 Nov 29	1116	0.81×0.28; 12	13

Table 2. Annual parallax and absolute proper motion of the spots which appeared in all five epochs. Coordinates are relative to the phase center ($02^h43^m28.5680^s$, $62°57'08.388''$) at epoch 2006.5. Column five lists the parallax estimates. Columns six and seven give the motion on the plane of the sky along the right ascension and declination, respectively. $\mu_{\rm RA}$ is the true RA motion multiplied by cos(Dec.).

Feature	$V_{\rm LSR}$ (km s^{-1})	ΔRA (mas)	ΔDec (mas)	π (mas)	$\mu_{\rm RA}$ (mas year^{-1})	$\mu_{\rm Dec}$ (mas year^{-1})
1	-66.42	-69.34	-203.72	0.168±0.006	−1.36±0.02	0.58±0.03
1	-66.63	-69.34	-203.72	0.180±0.009	−1.37±0.02	0.60±0.02
1	-66.84	-69.35	-203.72	0.156±0.008	−1.34±0.02	0.63±0.03
1	-67.05	-69.36	-203.73	0.160±0.006	−1.36±0.02	0.56±0.03
1	-67.26	-69.36	-203.73	0.176±0.003	−1.37±0.03	0.57±0.01
1	-67.47	-69.37	-203.72	0.162±0.009	−1.36±0.02	0.62±0.03
1	-67.68	-69.38	-203.72	0.170±0.006	−1.37±0.02	0.61±0.02
1	-67.89	-69.39	-203.73	0.166±0.007	−1.37±0.02	0.59±0.02
1	-68.10	-69.40	-203.72	0.161±0.009	−1.36±0.02	0.61±0.03
1	-68.31	-69.40	-203.73	0.165±0.007	−1.36±0.02	0.59±0.02
1	-68.53	-69.41	-203.73	0.170±0.007	−1.37±0.02	0.58±0.02
1	-68.74	-69.41	-203.74	0.166±0.006	−1.36±0.02	0.57±0.01
1	-68.95	-69.42	-203.74	0.168±0.006	−1.37±0.02	0.55±0.01
1	-69.16	-69.43	-203.74	0.164±0.009	−1.36±0.03	0.56±0.02
1	-69.37	-69.43	-203.74	0.164±0.009	−1.35±0.03	0.57±0.02
1	-69.58	-69.43	-203.74	0.176±0.004	−1.37±0.03	0.56±0.01
1	-69.79	-69.44	-203.74	0.170±0.006	−1.36±0.02	0.57±0.01
1	-70.00	-69.44	-203.74	0.170±0.006	−1.35±0.02	0.58±0.01
1	-70.21	-69.45	-203.74	0.173±0.004	−1.35±0.03	0.59±0.01
1	-70.42	-69.45	-203.74	0.163±0.006	−1.34±0.02	0.61±0.02
1	-70.63	-69.45	-203.74	0.167±0.004	−1.35±0.02	0.60±0.01
1	-70.84	-69.45	-203.74	0.166±0.006	−1.35±0.02	0.60±0.02
1	-71.05	-69.45	-203.75	0.166±0.002	−1.34±0.02	0.61±0.01
1	-71.26	-69.46	-203.75	0.160±0.007	−1.33±0.02	0.63±0.02
1	-71.47	-69.46	-203.75	0.156±0.009	−1.33±0.02	0.63±0.03
1	-71.68	-69.47	-203.75	0.156±0.008	−1.33±0.02	0.62±0.02
1	-71.90	-69.47	-203.76	0.153±0.010	−1.32±0.02	0.63±0.03
1	-72.11	-69.48	-203.77	0.148±0.011	−1.32±0.03	0.60±0.05
1	-72.32	-69.49	-203.76	0.176±0.002	−1.36±0.03	0.60±0.01
1	-72.53	-69.49	-203.77	0.168±0.007	−1.34±0.03	0.58±0.02
	Average			0.166±0.001 (0.007)	−1.35±0.004 (0.02)	0.59±0.004 (0.02)
	Combined fit			0.164±0.0014		
2	-72.53	-28.65	-141.63	0.155±0.007	−1.25±0.02	0.79±0.07
2	-72.74	-28.67	-141.68	0.152±0.008	−1.17±0.02	0.83±0.03
2	-72.95	-28.72	-141.71	0.176±0.006	−1.18±0.03	0.80±0.01
2	-73.16	-28.77	-141.74	0.176±0.005	−1.20±0.03	0.81±0.01
2	-73.37	-28.82	-141.76	0.173±0.005	−1.21±0.02	0.79±0.01
2	-73.58	-28.86	-141.77	0.162±0.002	−1.17±0.03	0.82±0.01
2	-73.79	-28.88	-141.78	0.151±0.010	−1.11±0.02	0.84±0.06
	Average			0.164±0.004 (0.011)	−1.18±0.02 (0.04)	0.81±0.01 (0.02)
	Combined fit			0.163±0.004		
3	-74.63	-24.93	-141.84	0.191±0.012	−1.39±0.04	1.06±0.07
3	-74.85	-24.88	-141.85	0.158±0.016	−1.20±0.04	1.07±0.04
3	-75.06	-24.86	-141.87	0.150±0.014	−1.18±0.04	1.05±0.04
3	-75.27	-24.86	-141.87	0.158±0.015	−1.22±0.04	1.05±0.04

Table 2—Continued

Feature	V_{LSR} ($km\,s^{-1}$)	ΔRA (mas)	ΔDec (mas)	π (mas)	μ_{RA} ($mas\,year^{-1}$)	μ_{Dec} ($mas\,year^{-1}$)
3	-75.48	-24.85	-141.87	0.170±0.017	−1.29±0.05	1.03±0.04
3	-75.69	-24.87	-141.87	0.174±0.022	−1.36±0.07	1.02±0.05
3	-75.90	-24.89	-141.87	0.140±0.014	−1.39±0.07	1.07±0.03
	Average			0.163±0.006 (0.016)	−1.29±0.03 (0.08)	1.05±0.01 (0.02)
	Combined fit			0.164±0.007		
Average				0.164±0.001 (0.0015)	−1.27±0.05 (0.09)	0.82±0.13 (0.23)
Combined fit all				0.164±0.0016		

Table 3. Positions and internal proper motions of all detected maser features relative to the reference feature 2.

Feature	V_{LSR} ($km\,s^{-1}$)	ΔRA (mas)	ΔDec (mas)	μ_{RA} ($mas\,year^{-1}$)	μ_{Dec} ($mas\,year^{-1}$)
1	−70.6	−40.654	−61.958	−0.19±0.01	−0.20±0.01
2	−73.2	0.0	0.0	0.0	0.0
3	−75.3	3.911	−0.152	−0.08±0.03	0.20±0.01
4	−62.2	26.946	225.653	−0.98±0.03	−0.29±0.04
5	−66.0	26.794	226.021	−0.90±0.05	−0.16±0.11
6	−75.1	71.988	121.071	0.43±0.04	−1.42±0.05
7	−74.6	72.074	121.087	0.04±0.07	−1.24±0.07
8	−74.8	72.715	120.628	−0.02±0.03	−1.19±0.08
9	−71.3	−41.526	−63.426	−0.05±0.09	0.04±0.09
10	−73.6	7.187	−2.340	0.66±0.01	0.01±0.03
11	−73.8	7.062	−2.330	0.66±0.01	−0.01±0.03
12	−75.5	5.558	−0.486	0.17±0.01	0.43±0.05
Average				−0.02±0.15 (0.5)	−0.35±0.18 (0.6)